

Particle size effects on the structure and emission of $\text{Eu}^{3+}:\text{LaPO}_4$ and EuPO_4 phosphors

Tamara Gavrilović^{a,b}, Jovana Periša^a, Jelena Papan^a, Katarina Vuković^a, Krisjanis Smits^b,
Dragana J. Jovanović^{a,*}, Miroslav D. Dramićanin^{a,*}

^a Vinča Institute of Nuclear Sciences, University of Belgrade, P.O. Box 522, 11001 Belgrade, Serbia

^b Institute of Solid State Physics, University of Latvia, 8 Kengaraga Street, Riga LV-1063, Latvia

ARTICLE INFO

Keywords:

Eu^{3+} -doped LaPO_4
Solid state synthesis
Co-precipitation
Reverse micelle
Colloids

ABSTRACT

This paper provides the detailed study of (nano)particle's size effect on structural and luminescent properties of $\text{LaPO}_4:\text{Eu}^{3+}$ synthesized by four different methods: high temperature solid-state, co-precipitation, reverse micelle and colloidal. These methods delivered monoclinic monazite-phase submicron particles (> 100 nm), 4×20 nm nanorods and 5 nm spheres (depending on the annealing temperature), 2×15 nm nanorods, and ultra-small spheres (2 nm), respectively. The analysis of emission intensity dependence on Eu^{3+} concentration showed that quenching concentration increases with a decrease of the particle size. The critical distance for energy transfer between Eu^{3+} ions is found to be 18.2 Å, and the dipole-dipole interaction is the dominant mechanism responsible for the concentration quenching of emission. With the increase in Eu^{3+} concentration, the unit-cell parameter slightly increases to accommodate larger Eu^{3+} ions at sites of smaller La^{3+} ions. Photoluminescent emission spectra presented four characteristic bands in the red spectral region: at 592 nm (${}^5\text{D}_0 \rightarrow {}^7\text{F}_1$), at 612 nm (${}^5\text{D}_0 \rightarrow {}^7\text{F}_2$), at 652 nm (${}^5\text{D}_0 \rightarrow {}^7\text{F}_3$) and at 684 nm (${}^5\text{D}_0 \rightarrow {}^7\text{F}_4$), while in small colloidal nanoparticles additional emission bands from host defects appear at shorter wavelengths. Intensities of f-f electronic transitions change with particles size due to small changes in symmetry around europium sites, while emission bandwidths increase with the reduction of particle size due to increased structural disorder. Judd-Ofelt analysis showed that internal quantum yield of Eu^{3+} emission is strongly influenced by particle's morphology.

1. Introduction

In recent times, much attention has been focused on luminescent nanomaterials due to their unique chemical, structural and physico-chemical properties, and their prospective applications in manufacturing nanoscale electronic, optoelectronic and sensing devices [1–3]. Luminescent nanomaterials are used in everyday life due to their employment in distinct fields of science and technology, like cathode ray tubes (CRTs), flat panel display devices, temperature sensors, lasers, solar-cells, biological imaging, solid-state lighting but also as carriers for miscellaneous therapeutic drugs [4,5]. The production and marketing of cost-effective, energy-saving and size-reduced nanomaterials with different shapes are of major importance for a development of multifunctional optical, magnetic and electrical properties and functions and to unfold new domain of theoretical and technological importance [6,7]. It is well known that optical properties of luminescent materials depend on properties of the host material and the electronic structure and concentration of the rare-earth ions [8,9]. In case of

nanomaterials, optical properties are also influenced by the size and morphology of particles, generally showing reduced quantum efficiency of emission in small-size particles. Therefore, efforts in enhancing of emission intensities of rare-earth activated nanoparticles relay on the understanding of mechanisms responsible for this enhancement [10,11].

Lanthanide orthophosphates (LnPO_4) have several polymorphic forms: hexagonal, tetragonal, and monoclinic. Among them, monoclinic (monazite) phase of lanthanum phosphate (LaPO_4) is perchance the most studied one. Rare-earth doped LaPO_4 represents an important class of luminescent nanomaterials. An orthophosphate host has proven to be suitable for production of efficient down-shifting and up-conversion materials [12–14]. In addition, monazite LaPO_4 has attractive properties such as low water solubility [15], high chemical, thermal and photo-stability [16], and large index of refraction ($n = 1.85$) [17–19]. It can be easily doped with different trivalent lanthanide ions without need for the charge compensation due to the same valance and similar ionic radii between La and lanthanide dopants [20]. A great

* Corresponding authors.

E-mail addresses: draganaj@vinca.rs (D.J. Jovanović), dramican@vinca.rs (M.D. Dramićanin).

Table 1Literature review on methods of synthesis, morphologies, particle size and dopant's optimal concentration for rare-earth doped LaPO₄ particles.

Compound	Method of synthesis	Morphology	Size (diameter × length)	Optimal concentration
LaPO ₄	Hydrothermal [34]	spherical irregular grain-like nanorods	2 μm 50–250 nm 100 nm 500 nm	– – –
LaPO ₄ :Eu ³⁺	hydrothermal (strongly alkaline solution) [35] hydrothermal method (acidic solution) [35] hydrothermal [36] hydrothermal [37] combustion [38] oil-bath route [39] sol-gel [40] molten-salt [41] precipitation [42]	nanoparticles fibers microspheres rod-like spherical abundant irregular particles nanotube quasihexagonal nanowire	10–50 nm 5–20 nm × several micrometers 5–8 μm 10–20 nm × 100–600 nm 0.5–3 μm 700–1200 nm × 500–1000 nm 20–200 nm 300 nm 33 nm × 0.1–2 μm	5 mol% 5 mol% 5 mol% 14 mol% 5 mol% 20 mol% 5 mol% 8 mol% 15 mol%
LaPO ₄ :Sm ³⁺	co-precipitation [43] hydrothermal [44]	nanowires nanorods peanut-like	7–8 nm × several hundred nm 100–400 nm 100–120 nm × 200 nm	2 mol% 4 at%
LaPO ₄ :Dy ³⁺ LaPO ₄ :Er ³⁺	sol-gel [45] precipitation [46] solid-state [19]	cuboids nanoparticles bulk	10 nm 125 nm sub-μm to few μm	10 at% 3 mol% 0.05 mol%
LaPO ₄ :Tb ³⁺	microwave assisted co-precipitation [47] hydrothermal method [48] hydrothermal technique [49]	nanorods nanorods nanowires	10–15 nm × 300–800 nm 40–50 nm × 350–400 nm 7–20 nm × 2.5 μm	15 mol% 5 mol% 11 mol%
LaPO ₄ :Ce ³⁺	hydrothermal (EDTA assisted) [50]	rod-like peanut-like	80 nm × 400 nm 100–120 nm × 200 nm	20 mol%
LaPO ₄ :Ce ³⁺ /Tb ³⁺	hydrothermal [50] microwave-assisted co-precipitation [51]	bunch-like nanorods bundles	100 nm × 500 nm 60 nm × 300 nm	20 mol% Ce ³⁺ 15 mol% Tb ³⁺ 40 mol% Ce ³⁺ 20 mol% Tb ³⁺
LaPO ₄ :Pr ³⁺ LaPO ₄ :Gd ³⁺	spray pyrolysis [52] re-crystallization method [53] solid state [54] hydrothermal method [55]	hollow spheres irregular spherical spherical nanorods	50–100 nm 2–10 μm 0.2–2.0 μm 200–700 nm	2 mol% 0.04 mol% 0.5 mol% 3 mol%
LaPO ₄ :Nd ³⁺ LaPO ₄ :Er ³⁺ /Yb ³⁺	microwave [56] co-precipitation method [57]	agglomerates creating balls Rod-like	700 nm 30–50 nm	10 mol% 20 mol% Yb ³⁺ 1 mol% Eu ³⁺
LaPO ₄ :Tm ³⁺ @CNT	co-precipitation method [58]	–	–	–

number of methods has been developed for the synthesis of un-doped and lanthanide doped LaPO₄ such as: co-precipitation [21,22], sonochemical approach [23], combustion route [24], mechanical milling [25], electrospinning method [26], etc., (as it is given in Table 1). These methods provide LaPO₄ of different morphologies and particle size: nanoparticles (10–50 nm), microspheres (0.5–10 μm), hollow spheres (50–100 nm), nanorods (with diameter 10–80 nm and length 400–600 nm), short nanotubes, nanowires (of 5–35 nm diameter and length up to several micrometers), as well as particles with unusual morphologies such as the bunch-like (100 × 500 nm) and the peanut-like (100–120 × 200 nm).

Up to now, the size effect on photoluminescent properties of several different hosts doped with Eu³⁺ ions has been studied [27–29]. Mostly, the ratio of red (⁵D₀→⁷F₂) and orange (⁵D₀→⁷F₁) emission intensities has been observed to increase with the decrease of particle size. Herein, the goal was to thoroughly investigate the size effect on the structure and luminescence of LaPO₄:Eu³⁺ nanophosphors. Materials were prepared by four different methods of synthesis: solid-state, co-precipitation, reverse micelle and colloidal in accordance to the methods used for syntheses of the lanthanide-doped GdVO₄ [30–33]. The size effect on luminescent emission intensities and decays, structure, and morphology were analyzed by steady-state and time-resolved photoluminescence spectroscopy, X-ray diffraction, scanning and transmission electron spectroscopy, and diffuse reflection spectroscopy. In addition, Judd-Ofelt analysis of Eu³⁺ emission was performed to evaluate radiative properties of Eu³⁺ in different-size hosts.

2. Experimental

2.1. Materials and methods

The Eu³⁺-doped LaPO₄ and EuPO₄ nanoparticles (NPs) and nanorods (NRs) of different particle sizes were synthesized by four methods (colloidal, reverse micelle, co-precipitation and solid-state) by analogy to the methods presented in our previous papers [30–33]. All chemicals: lanthanum(III) oxide, La₂O₃ (99.99%, Alfa Aesar), europium(III) oxide, Eu₂O₃ (99.9%, Alfa Aesar), lanthanum(III) nitrate hexahydrate La(NO₃)₃ × 6H₂O (99.99%, Alfa Aesar), europium(III) nitrate hexahydrate, Eu(NO₃)₃ × 6H₂O (99.9%, Alfa Aesar), ammonium hydrogen phosphate, (NH₄)₂HPO₄ (98.0%, Alfa Aesar), Na₃C₆H₅O₇ × 2H₂O, trisodium citrate dihydrate (≥ 99%, Sigma Aldrich), cyclohexane, Triton X-100, and n-pentanol were of the highest purity commercially available and were used without further purification. Milli-Q deionized water (electrical resistivity = 18.2 MΩ cm⁻¹) was used as solvent.

2.2. The high-temperature solid-state method

The bulk Eu³⁺-doped LaPO₄ particles were prepared by a high-temperature solid-state method. In a typical synthesis, the La₂O₃ and Eu₂O₃ (in concentration ratio of 1, 2, 5, 10, 15 and 20 mol% Eu³⁺ with respect to La³⁺ ions) and (NH₄)₂HPO₄, were homogeneously mixed by dry grinding and heated for 1 h in open crucibles at 800 °C. The products were removed from the furnace, cooled down to room

temperature, finely ground, and reheated at 1100 °C for 3 h to complete the reaction. After that, the powder was homogeneously ground, washed with 2 M NaOH solution water, and methanol and was calcined at 1150 °C for 90 min to improve the crystallinity of material and to remove ligands attached to particle surfaces during the washing step. Throughout the manuscript, the samples prepared with solid state technique will be denoted as bulk, non-regular spheres (S-LaPO₄) with size more than 100 nm.

2.3. The co-precipitation method

The LaPO₄:x mol% Eu³⁺ (x = 1, 2, 5, 10, 15, 20) NRs were synthesized by chemical co-precipitation technique. Appropriate amount of (NH₄)₂HPO₄ was dissolved in water (pH = 12). A mixture of aqueous solutions of La(NO₃)₃ × 6H₂O and Eu(NO₃)₃ × 6H₂O (in concentration ratio of 1–20 mol% Eu³⁺ with respect to La³⁺ ions) was added dropwise in a (NH₄)₂HPO₄ solution. A formed milk-white opalescent precipitate of LaPO₄:Eu³⁺ was additionally heated and stirred at 60 °C for 1 h. The pH value of the milk-white suspension was about 9. The precipitate was separated from the suspension by centrifugation, and washed several times with distilled water to adjust the pH value to 7. Finally, the collected powder of LaPO₄:Eu³⁺ was dried at 60 °C in the air for 20 h (later in the text denoted as “as-prepared” sample). To improve their crystallinity and to get particles with different size and morphology, the as-prepared powder was additionally annealed at 600 °C for 2 h. Throughout the manuscript, the samples prepared with the co-precipitation technique will be denoted as nanorods 4 nm × 20 nm (P-LaPO₄-ap) and nanospheres 5 nm (P-LaPO₄-600C).

2.4. The reverse micelles method

The LaPO₄: x mol% Eu³⁺ (x = 1, 2, 5, 10, 15, 20, 30, 50, 75) and EuPO₄ stoichiometric compound with NRs morphology were synthesized by reverse micelles method. A typical synthesis performed at room temperature was as it follows. Three different solutions were prepared: *i*) an oil phase formed by mixing cyclohexane, Triton X-100, and *n*-pentanol in a corresponding volume ratio, *ii*) a mixture of aqueous solutions of La(NO₃)₃ × 6H₂O and Eu(NO₃)₃ × 6H₂O (in corresponding concentration ratio of Eu³⁺ ions with respect to La³⁺ ions), and *iii*) an aqueous solution of (NH₄)₂HPO₄. In the next step, the oil phase and solution of (NH₄)₂HPO₄ were mixed, and the solution containing La³⁺ (Eu³⁺) ions was added into the obtained mixture under continuous magnetic stirring. After 1 h of stirring at room temperature and 24 h aging, the white colloid dispersion containing reverse micelles was obtained. Then, methanol was added to destabilize the solution and the resulting precipitate was separated by centrifugation and washed several times by methanol and water. The collected precipitate was dried at 60 °C in the air for 20 h. Throughout the manuscript, the samples prepared with the reverse micelle technique will be denoted as nanorods, 2 nm × 15 nm (M-LaPO₄).

2.5. The colloidal synthesis

Colloidal LaPO₄:x mol%Eu³⁺ (x = 0, 1, 5, 10, 15, 20, 30, 50, 75) and EuPO₄ stoichiometric compound with NPs morphology were synthesized by analogy to the method presented in our previous paper based on the GdVO₄:Eu³⁺ [30]. In brief, the solution of trisodium citrate dihydrate was added drop by drop to the mixture of La(NO₃)₃ × 6H₂O and Eu(NO₃)₃ × 6H₂O solution in the stoichiometric ratio (solutions were mixed in corresponding concentration ratio of Eu³⁺ ions with respect to La³⁺ ions up to stoichiometric EuPO₄) at room temperature. The white precipitate consisting of the La³⁺ (Eu³⁺)-Cit³⁻-complex is formed, and then completely dissolved by a vigorous stirring and the addition of (NH₄)₂HPO₄ solution. Further, the resulting transparent solution was stirred for 1 h at room temperature. The dialysis against distilled water for 24 h was utilized for the removal of excess

ions. Powder samples were obtained by evaporation of aqueous colloidal solutions. Throughout the manuscript, samples prepared with the colloidal technique are denoted as nanoparticles, 2 nm (K-LaPO₄).

2.6. Characterization methods and instrumentation

Powder X-ray diffraction (XRD) measurements were performed on a Rigaku SmartLab diffractometer using Cu-K_{α1, 2} radiation (λ = 0.15405 nm). Diffraction data were recorded with a step size of 0.01° and a counting time of 1°/min over the 2θ range of 10–90°. Transmission electron microscopy (TEM) studies were made on a Tecnai G20 (FEI) operated at an accelerating voltage of 200 kV. For these measurements, ethanol was used to transfer powder samples to the grids, and ultrasonic bath to separate agglomerates. An ultrathin carbon film on holey carbon grids (Agar S187-4) were used to facilitate measurements of extremely small-size nanoparticles. Luminescence measurements were performed with an Fluorolog-3 Model FL3-221 spectrofluorometric system (Horiba JobinYvon) utilizing a 450 W Xenon lamp as an excitation source for steady-state emission measurements, and a Xenon–Mercury pulsed lamp for emission decay measurements.

3. Results and discussion

3.1. Morphology and structure of LaPO₄:Eu³⁺ particles

Morphologies of LaPO₄:5 mol% Eu³⁺ nanoparticles (NPs) obtained by four different methods were studied by TEM and results are given in Fig. 1. TEM image of NPs in colloidal form shows ultra-small crystallites of approximately 2 nm in diameter (Fig. 1a). This finding is consistent with the crystallite size evaluated from the XRD measurement. It is interesting to note that similar values of the crystalline domain size and the microscopically estimated average particle size indicate that each particle consists of a single crystallite.

Short nanorods (NRs) of approximately 2 nm × 15 nm (*d* × *l*) and 4 nm × 20 nm (*d* × *l*) in size are obtained by reverse micelle and co-precipitation methods, respectively (Fig. 1b and c). The sample obtained by co-precipitation method additionally annealed at 600 °C shows single spherical particles about 5 nm in size (Fig. 1d). TEM image of the bulk sample shows that particles have multi-peak size distribution and powder is composed of crystallites/particles larger than 100 nm and could be noted as bulk material (Fig. 1e).

3.1.1. The size effect on structural properties of LaPO₄:Eu³⁺ particles

LaPO₄ crystallizes in a pure monoclinic monazite phase of a space group *P*121/*m*1 (ICDD card no. 90001647). In the LaPO₄ crystal lattice, lanthanum ions are coordinated with nine oxygen atoms forming polyhedrons (LaO₉) that share corner with PO₄ tetrahedra in which all four P–O bonds are equivalent. [59] X-ray diffraction patterns of LaPO₄:5 mol% Eu³⁺ samples having particles of different sizes are shown in Fig. 2. Typical X-ray diffraction patterns of all five series of samples doped with different concentrations of Eu³⁺ ions are shown in Supporting information file (Figs. S1–S5).

X-ray patterns are characterized with broad diffraction peaks which indicate samples with a quite small crystallite size and, possible, containing an amorphous phase. The presence of impurity could not be excluded solely from XRD patterns due to broad diffraction peaks which could conceal diffraction peaks of impurity phases. However, photoluminescence measurements, discussed later in the text, revealed no emissions that could be ascribed to Eu³⁺ located in different hosts than LaPO₄. Structural parameters of all LaPO₄:5 mol% Eu³⁺ samples were derived by the Rietveld refinement of XRD data, and results of the fitting are summarized in Table 2. Microstrain values range from 0.09% to 1.64% and suggest a good ion ordering in the nanocrystals. The average crystallite size, obtained from the Rietveld analysis, are in the 2.3–50.6 nm range, depending on the method of synthesis. The particle

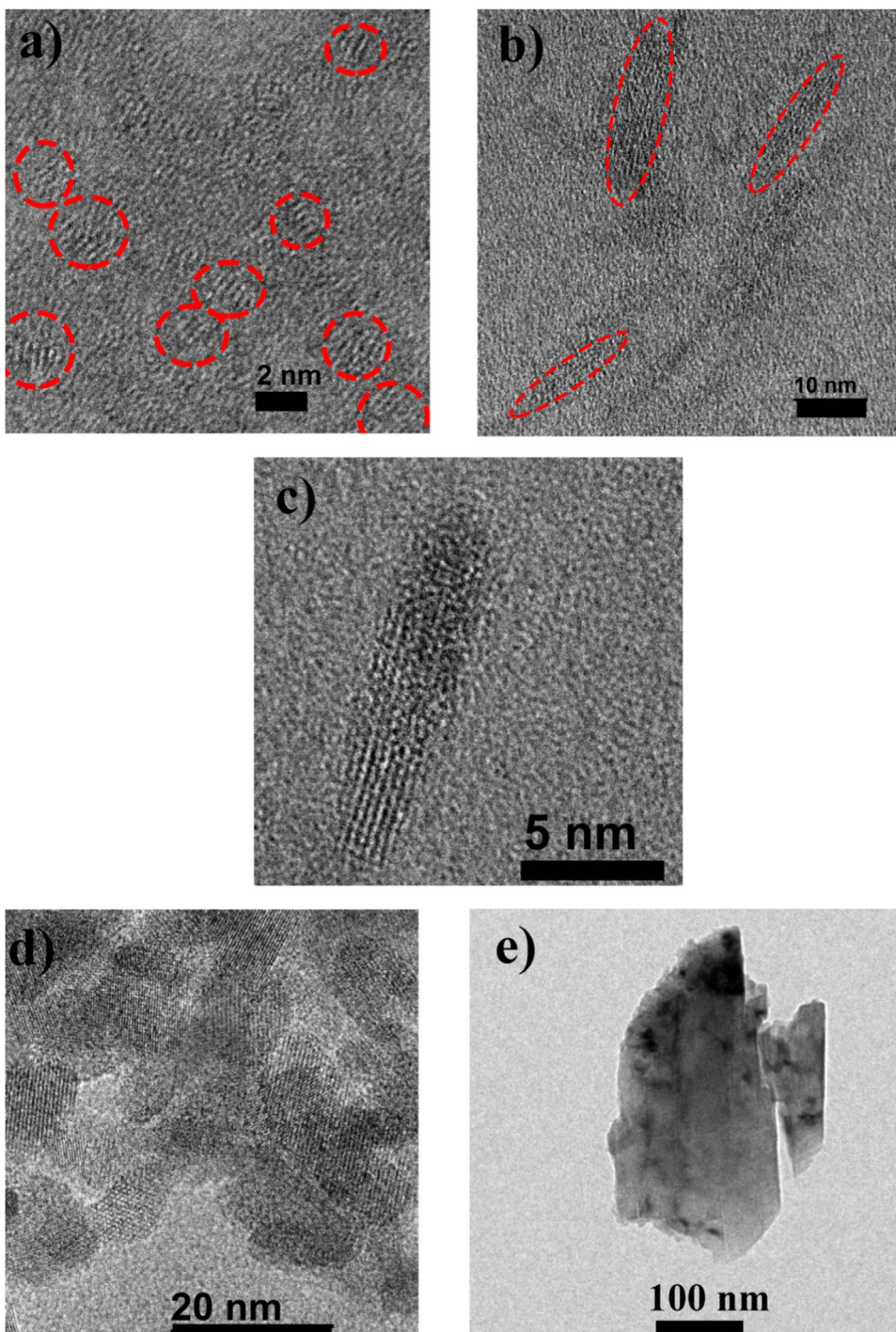


Fig. 1. TEM images of $\text{LaPO}_4:5 \text{ mol\% Eu}^{3+}$ nanoparticles obtained by four different methods: a) colloidal route; b) reverse micelles; c) co-precipitation (without annealing); d) co-precipitation (with annealing at $T = 600 \text{ }^\circ\text{C}$) and e) solid state reaction at high temperature.

sizes assessed by TEM are similar to the crystallite size obtained from XRD measurements for all nanoparticles, excluding bulk material, suggesting that each small particle comprises a single crystallite.

3.2. Luminescence properties of $\text{LaPO}_4:\text{Eu}^{3+}$ and EuPO_4 particles

3.2.1. Photoluminescence spectra and emission decays

For comparison, emission spectra (excited at 393 nm) of $\text{LaPO}_4:10 \text{ mol\% Eu}^{3+}$ samples obtained by different methods of synthesis are given in Fig. 3a.

Emission from ${}^5\text{D}_0 \rightarrow {}^7\text{F}_1$ magnetic-dipole electronic transition centered 592 nm is dominant one for all samples except for ultrasmall (2 nm) NPs. In addition, emission spectra show three strong bands,

centered at 612, 652 and 684 nm, from ${}^5\text{D}_0 \rightarrow {}^7\text{F}_2$, ${}^5\text{D}_0 \rightarrow {}^7\text{F}_3$ and ${}^5\text{D}_0 \rightarrow {}^7\text{F}_4$ transitions, respectively. Emission bandwidths are much larger in case of nanoparticles than for their bulk counterparts due to the increased structural disorder in nanoparticles. In bulk $\text{LaPO}_4:\text{Eu}^{3+}$, the europium site has C1 symmetry [60]. Ultrasmall NPs (2 nm) and short nanorods (2 nm \times 15 nm) show additional broad emission bands in the visible spectral region. The emission spectrum of short nanorods shows one broad band that could be attributed to PO_4^{3-} groups. The emission spectrum of ultra-small (2 nm) $\text{LaPO}_4:\text{Eu}^{3+}$ NPs shows two intense broad bands centered at 459 nm (blue emission) and 550 nm (green emission). These emissions can be attributed to defect emissions of host material. Due to large surface-to-volume ratio and the substantial number of surface defects, the symmetry around Eu^{3+} ions is

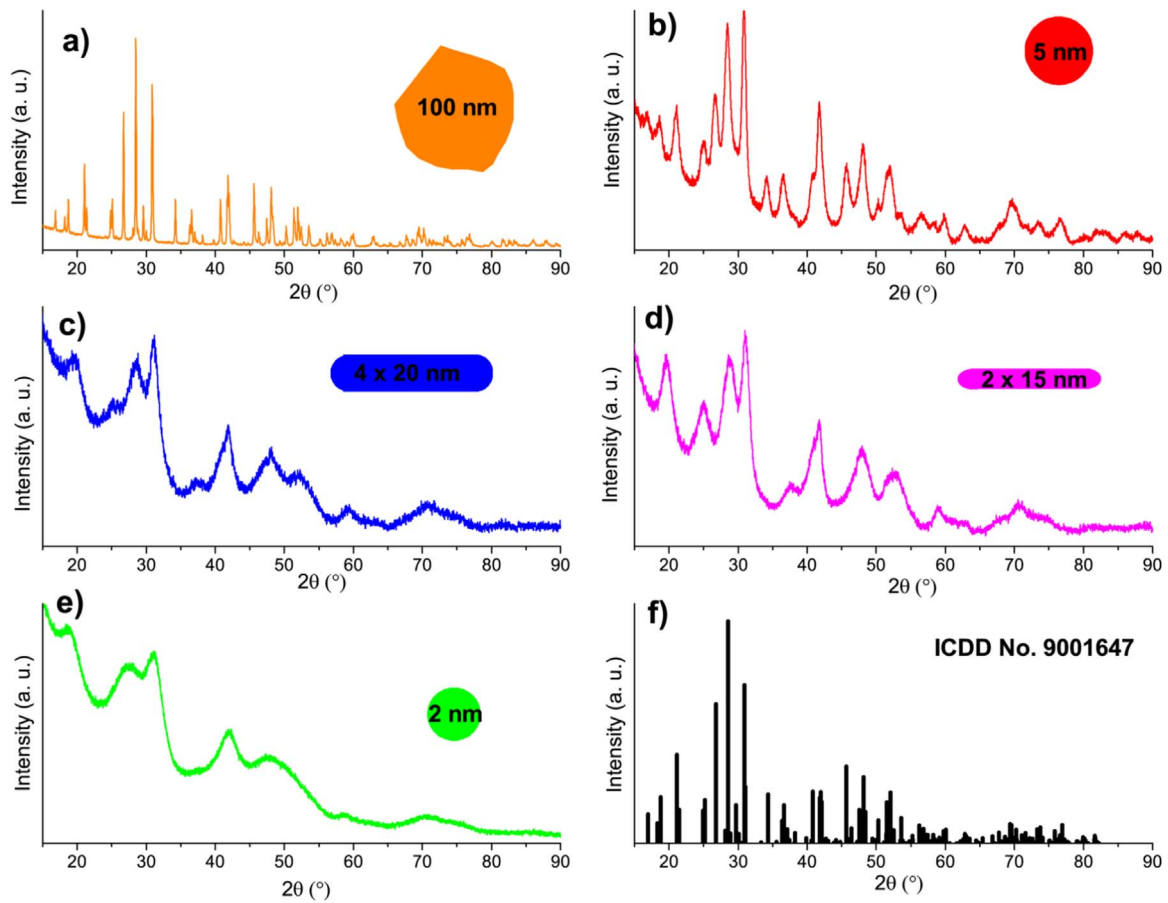


Fig. 2. X-ray diffraction patterns of $\text{LaPO}_4:5 \text{ mol\% Eu}^{3+}$: a) bulk (nanoparticles > 100 nm), b) nanoparticles (5 nm), c) nanorods (4 nm \times 20 nm), d) nanorods (2 nm \times 15 nm) and colloidal nanoparticles (2 nm).

different than in larger NPs. In this case, the dominant emission is centered at 612 nm, and is a result of ${}^5\text{D}_0 \rightarrow {}^7\text{F}_2$ transition. To assure that broad bands centered at 459 nm and 550 nm originate from host defects, an emission spectrum is taken from the un-doped colloidal LaPO_4 NPs, Fig. 3b. This spectrum displays bands at 459 nm and 550 nm, but no emissions from the Eu^{3+} . Blue emission is caused by deep levels and self-trapped excited luminescence, while the green emission can be attributed to the recombination of electrons of ionized oxygen vacancies with photogenerated holes [61]. High surface-to-volume ratio of ultra-small NPs plays a major role in the concentration of ionized oxygen vacancies, and the charge state of these defects promotes the green emission. Emission decay curves are measured for the ${}^5\text{D}_0 \rightarrow {}^7\text{F}_1$

transition at 592 nm; decay curves obtained with $\text{LaPO}_4:10 \text{ mol\% Eu}^{3+}$ samples are shown in Fig. 4. Emission decays of bulk material and 5 nm NPs were fitted by a single exponential function. However, decay curves for 2 nm NPs and 2 nm \times 15 nm and 4 nm \times 15 nm NRs are not single-exponential, and were fitted by a double exponential function. The average lifetime, τ_{avg} , was calculated using parameters of a double exponential fit from the following equation:

$$\tau_{\text{avg}} = \frac{A_1 \tau_1^2 + A_2 \tau_2^2}{A_1 \tau_1 + A_2 \tau_2} \quad (1)$$

where A_1 and A_2 are pre-exponential factors; the τ_1 and τ_2 are lifetime values. The obtained values of lifetime given in Table 3 were used for

Table 2
Selected structural parameters of $\text{LaPO}_4:5 \text{ mol\% Eu}^{3+}$ nanophosphors obtained by Rietveld refinement of XRD data.

Parameters	nanoparticles (2 nm)	nanorods (2 \times 15 nm)	nanorods (4 \times 20 nm)	nanoparticles (5 nm)	particles > 100 nm
CS (nm)	2.297 (3)	2.4647 (10)	2.647 (15)	5.16 (3)	50.7 (6)
a (\AA)	7.0007 (5)	6.878 (14)	6.956 (8)	6.845 (3)	6.83225 (19)
b (\AA)	6.911 (5)	7.070 (13)	7.040 (8)	7.075 (3)	7.0676 (2)
c (\AA)	6.503 (4)	6.515 (11)	6.498 (8)	6.501 (3)	6.50359 (18)
V (\AA^3)	314.63	316.81	318.21	314.83	314.04
Strain (%)	1.64 (6)	0.54 (4)	0.58 (5)	0.51 (6)	0.09 (2)
^a Rwp (%)	4.13	11.80	6.80	4.75	5.77
^b Rp (%)	3.21	9.23	5.15	3.66	4.21
^c Re (%)	1.73	8.88	3.80	3.78	3.67
^d GOF	2.38531	1.3292	1.7916	1.2574	1.5745

^a The profile factor (Rp).

^b The weighted profile factor (Rwp).

^c The expected weighted profile factor (Re).

^d The goodness of fit (GOF).

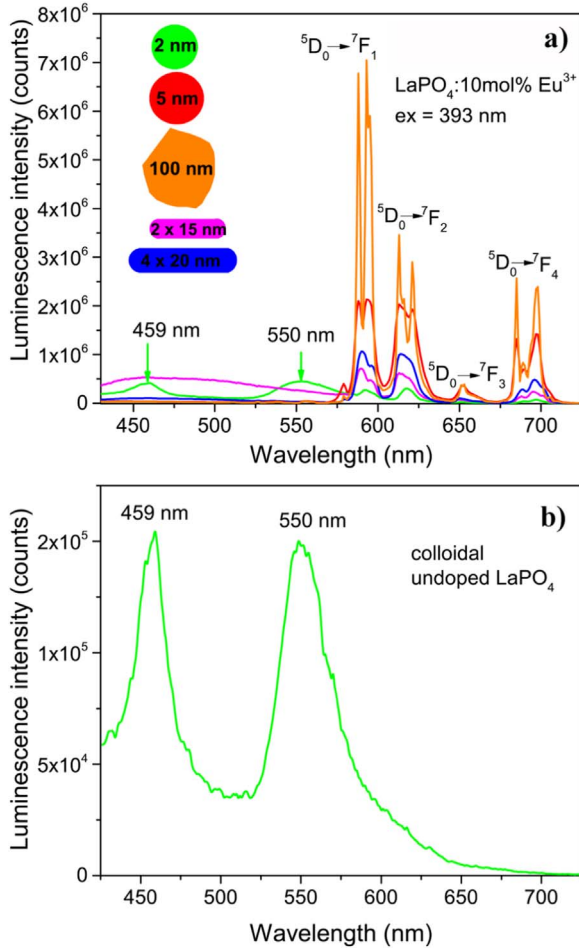


Fig. 3. a) Emission spectra of $\text{LaPO}_4:10 \text{ mol\% Eu}^{3+}$ nanoparticles obtained by different synthesis methods: reverse micelle, co-precipitation (without annealing), co-precipitation (annealed at 600°C), and solid state recorded under 393 nm excitation wavelength. b) Emission spectrum of colloidal un-doped LaPO_4 nanoparticles.

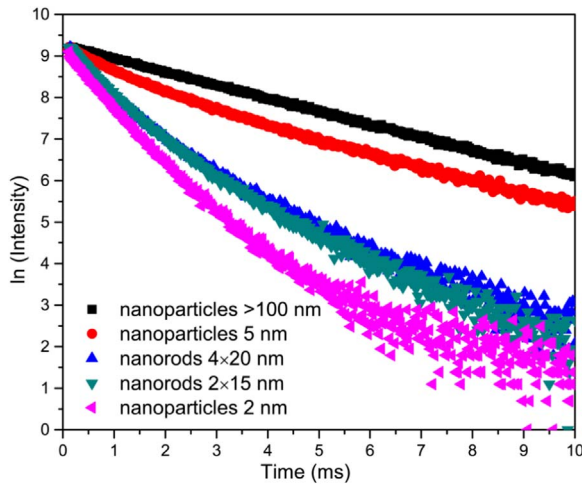


Fig. 4. Fluorescence decay curves of Eu^{3+} ions for the transition ${}^5\text{D}_0 \rightarrow {}^7\text{F}_1$ at 592 nm for different size of $\text{LaPO}_4:10 \text{ mol\% Eu}^{3+}$ systems.

determination of photophysical properties using Judd-Ofelt analysis (see text in Section 3.2.3.). A difference in model of fitting with reduced particle size could be explained by an increasing concentration of the ions (dopant) on the surface of NPs, i.e. with different decays of the Eu^{3+} ions at the surface and Eu^{3+} ions in the volume of the nanoparticles [62].

3.2.2. The concentration quenching of Eu^{3+} emission

Emission intensity dependences on Eu^{3+} concentration in $\text{LaPO}_4:\text{Eu}^{3+}$ particles of different sizes are given in Supporting information file (Figs. S6–S10). These spectra reveal that maximal emission intensity is achieved with the 10 mol% doping in cases of bulk material, 5 nm NPs and 4 nm \times 20 nm NRs; the further increase in Eu^{3+} concentration causes intensity decrease due to the concentration quenching. In the case of ultra-small (2 nm) nanoparticles and shorter nanorods (2 nm \times 15 nm) no concentration quenching was observed up to Eu^{3+} concentrations which correspond to the stoichiometric material (EuPO_4). The absence of concentration quenching in ultra-small NPs may be attributed to the phonon confinement, which fosters non-radiative decays during energy migration between Eu^{3+} ions.

To further investigate the nature of concentration quenching in particles, the critical transfer distance (R_c) of $\text{Eu}^{3+}-\text{Eu}^{3+}$ pairs is calculated using Blasse's equation:

$$R_c = 2 \left(\frac{3V}{4\pi X_c N} \right)^{1/3} \quad (2)$$

Here, X_c is the critical concentration, N is the number of Z ions in the unit cell, and V is the volume of the unit cell. The X_c is 0.1 (which equals 10 mol%, see Fig. 5) and Z is 1, and values of V are taken from Table 2 after Rietveld refinement of XRD data.

The calculated critical distance for energy transfer R_c is 18.2 \AA . Three types of nonradiative energy transfer can be considered, the exchange interaction, the radiation reabsorption, and the multipole–multipole interaction. Small overlap between excitation and emission spectra implies that the radiation reabsorption is not a major mechanism responsible for the concentration quenching. The exchange interaction is dominant when critical distance between donor and acceptor ions is smaller than 5 \AA . Here, the critical distance is around 18 \AA , which is larger than 5 \AA , which implies that energy transfer mechanism is a multipole–multipole interaction. This interaction may be of dipole–dipole, dipole–quadrupole, and quadrupole–quadrupole type, and the type can be determined from the Van Uitert's equation:

$$\frac{1}{x} = K [1 + \beta(x)^Q]^{-1} \quad (3)$$

where x stands for Eu^{3+} concentrations equal or higher than critical concentration, I is the emission intensity, while K and β are constants. Depending on the type of interaction, Q can take values of 6, 8 and 10, for the dipole–dipole, dipole–quadrupole, and quadrupole–quadrupole interaction, respectively. From the $\log(I/x)$ vs $\log(x)$ plots, shown as insets in Fig. 5a–c, Q values were found to be 4.65, 4.11 and 4.44 for bulk (nanoparticles $> 100 \text{ nm}$), nanoparticle (5 nm) and nanorods (4 nm \times 20 nm), respectively. Therefore, concentration quenching of Eu^{3+} emission is due to dipole–dipole interaction.

Surface to volume ratio in NPs has a significant effect on their properties, and it is well-known that the surface to volume ratio increases with the reduction of radius of spherical NPs (see Fig. 6a). Also, as particle size decreases, a greater portion of the atoms resides on the particle surface. Here, in case a 2 nm NPs 75% of its atoms are on the particle surface, for 5 nm NPs 30%, while bulk ($> 100 \text{ nm}$) particles have $< 1.5\%$ of their atoms on the surface. In cases of 2 nm \times 15 nm and 4 nm \times 20 nm NRs, 56.5% and 30% of their atoms are located at the surface, respectively. One should note that particles having $> 50\%$ atoms on the surface (2 nm NPs and 2 nm \times 15 nm NRs) did not show concentration quenching of emission, i.e. they could be heavily doped with Eu^{3+} , up to stoichiometric EuPO_4 NPs. When such high amount of dopant ions resides on the surface, the surface quenching of emission is considerable stronger than the concentration quenching, so one is able to observe only the increase in emission intensity due to larger number of emission centers upon the increase in dopant concentration. The dependence of the critical concentration of Eu^{3+} ions for different sizes of $\text{LaPO}_4:\text{Eu}^{3+}$ NPS is given in the Fig. 6b.

Table 3

Calculated Judd-Ofelt intensity parameters, radiative and non-radiative transition rates, experimentally measured lifetimes, quantum efficiencies and asymmetry ratios of Eu^{3+} emission from $\text{LaPO}_4:10 \text{ mol\% Eu}^{3+}$ NPs with different size.

	$\Omega_2 (10^{-20} \text{ cm}^2)$	$\Omega_4 (10^{-20} \text{ cm}^2)$	$A (s^{-1})$	$A_{NR} (s^{-1})$	$\tau (10^{-3} \text{ s})$	$\eta (\%)$	R
Particles (> 100 nm)	1.06	1.70	216	85	3.31	72	0.64
Nanoparticles (5 nm)	2.11	2.65	319	90	2.44	78	1.27
Nanorods (4 nm × 20 nm)	1.97	2.01	283	63	2.89	82	1.19
Nanorods (2 nm × 15 nm)	2.01	2.21	291	18	3.23	94	1.21
Nanoparticles (2 nm)	1.70	0.84	229	227	2.19	50	1.02

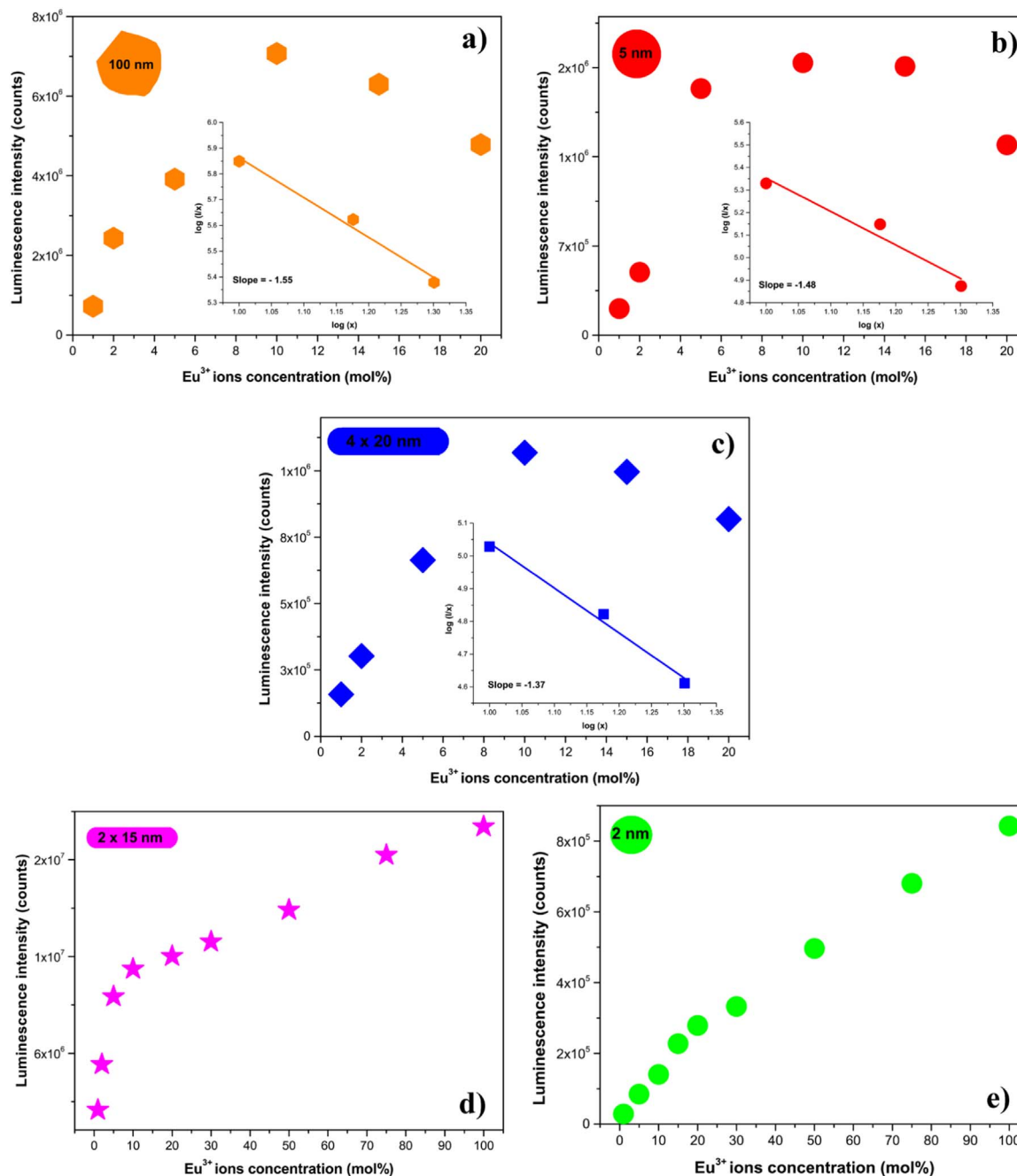


Fig. 5. Dependence of luminescence intensity of ${}^5\text{D}_0 \rightarrow {}^7\text{F}_1$ (592 nm) transition on concentration ($x \text{ mol\%}$) Eu^{3+} ions for: a) bulk (nanoparticles > 100 nm); b) nanoparticles (5 nm); c) nanorods (4 nm × 20 nm); d) nanorods (2 nm × 15 nm); e) nanoparticles (2 nm) under excitation wavelength at 393 nm; Insets in Figures a)–c) show the dependence of $\log(I/x)$ vs $\log(x)$ plot for $x \geq 10 \text{ mol\%}$.

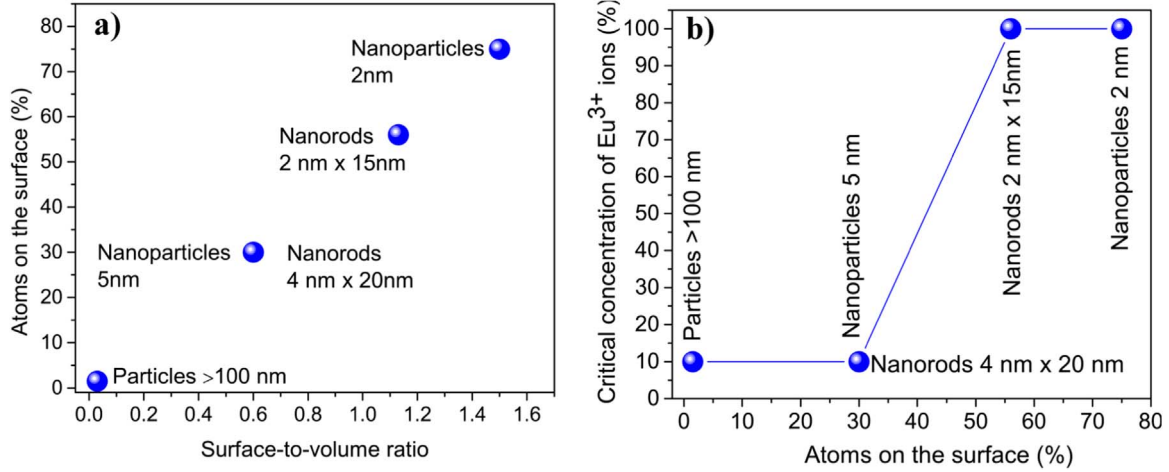


Fig. 6. Dependence of: a) Number of atoms on the surface vs surface-to volume ratio and b) The critical concentration of Eu^{3+} ions vs atoms on the surface for different sizes of $\text{LaPO}_4:\text{Eu}^{3+}$ nanoparticles.

3.2.3. Judd-Ofelt analysis

The Judd Ofelt (JO) analysis [63,64] has been applied to quantitatively describe optical properties of $\text{LaPO}_4:\text{Eu}^{3+}$ particles, from micro- to nanodimensions. In the framework of this theory, the dipole strengths of transitions are described by three phenomenological parameters Ω_λ ($\lambda = 2, 4, 6$) with the following equation [65]:

$$\Omega_\lambda = \frac{D_{MD}\nu_\lambda^3}{e^2\nu_\lambda^3} \frac{9n^3}{n(n^2+2)^2|\langle\Psi J||U^{(\lambda)}||\Psi'J'\rangle|^2} \frac{S(^5D_0 \rightarrow ^7F_\lambda)}{S(^5D_0 \rightarrow ^7F_\lambda)} \quad (4)$$

where ν_λ represents the barycentre of the transition, and $|\langle\Psi J||U^{(\lambda)}||\Psi'J'\rangle|^2$ are squared reduced matrix elements ($|\langle\Psi J||U^{(2)}||\Psi'J'\rangle|^2 = 0.0032$, $|\langle\Psi J||U^{(4)}||\Psi'J'\rangle|^2 = 0.0023$, $|\langle\Psi J||U^{(6)}||\Psi'J'\rangle|^2 = 0.0002$) [66]. In the case of Eu^{3+} , because only diagonal elements of the unit tensor operators between the wave functions of its electron configuration are not zero, the emission spectrum provides sufficient data for the evaluation of JO intensity parameters Ω_λ ($\lambda = 2, 4, 6$). In this case, one should consider the intensity of the $^5D_0 \rightarrow ^7F_1$ magnetic dipole transition as a reference for transitions originating from the 5D_0 excited state [67]. According to Ref. [68], magnetic dipole transition has the value of 57.34 s^{-1} for the $50(\text{NaPO}_3)_6 + 10\text{TeO}_2 + 20\text{AlF}_3 + 19\text{LiF} + \text{Eu}_2\text{O}_3$ glass with refractive index 1.591. Taking this value as a reference and with a well-known correction factor of $(n/1.591)^3$, which can be derived from the general equations for the magnetic dipole transition probability rate [69,70], we obtained the value of 42.85 s^{-1} (here $n = 1.85$ is the refractive index of LaPO_4 , taken from the literature) [17].

Judd-Ofelt parameters are further used for the calculation of radiative transitions probabilities:

$$A(\Psi J; \Psi' J') = \frac{64\pi^4 e^2}{3h(2J+1)\lambda^3} \left[n \left(\frac{n^2+2}{9} \right)^2 D_{ED} + n^2 D_{MD} \right] \quad (5)$$

where h denotes Planck constant ($6.63 \times 10^{-27} \text{ erg s}$), $2J + 1$ is the degeneracy of the initial state, n is the refractive index and e is charge of electron, and D_{MD} and D_{ED} are electric and magnetic dipole strengths, respectively.

By expressing the emission intensities in terms of the integrated areas, S , under the emission bands, radiative emission probabilities can be calculated from the following equation [65].

$$A_{2,4}(^5D_0 \rightarrow ^7F_{2,4,6}) = A(^5D_0 \rightarrow ^7F_1) \times \frac{S(^5D_0 \rightarrow ^7F_{2,4})}{S(^5D_0 \rightarrow ^7F_1)} \quad (6)$$

The total radiative emission probability, A_R , represents the sum of all radiative transitions probabilities:

$$A_R = \sum_{\lambda=1,2,4,6} A_\lambda \quad (7)$$

The radiative lifetime (τ_R) is given by the reciprocal of the total radiative decay rate (A_R). Using calculated lifetime values and total radiative transition probability we can calculate non-radiative probability A_{NR} as:

$$A_{NR} = \frac{1}{\tau} - A_R \quad (8)$$

and the emission quantum efficiency η is:

$$\eta = \frac{A_R}{A_R + A_{NR}} \quad (9)$$

Comparison of emission characteristics of Eu^{3+} in different size LaPO_4 particles (doped with the same amount of Eu^{3+} , 10 mol%) is done on account calculations performed with afore explained Judd-Ofelt analysis, Table 3.

The Ω_2 parameter is sensitive to the local structure and composition of the host material and can be associated with the asymmetry and covalence of the rare-earth site [65,71,72], while Ω_4 parameter can be related to the viscosity and rigidity. If one use Ω_2 to assess the magnitude of covalence between Eu^{3+} and surrounding ligands (the larger the Ω_2 , the stronger the covalence), it is possible to conclude that covalence increases with reduction of particles size. However, one should note that there are number of competing mechanisms for induced electric dipole transitions, so the dominant mechanism for such behavior cannot be determined from the single parameter. One can notice that the values of Ω_2 and Ω_4 constantly increase with the decrease of particle size, except for the smallest ones of 2 nm in diameter. Therefore, it is possible to conclude that local environments of Eu^{3+} ions in LaPO_4 crystal host undergo constant small changes as dimensions of crystal host are reduced. The relatively small value of Ω_2 indicates a relatively high symmetry at the Eu^{3+} site, which is the highest for the largest particles prepared by solid state method. This finding agrees with trend in values of the luminescence intensity ratio, $R = I(^5D_0 \rightarrow ^7F_2)/I(^5D_0 \rightarrow ^7F_1)$, which can be considered as indicative of the asymmetry of the coordination environment around the Eu^{3+} ion. Hence, the reduction of particle size obviously affects the local environment of Eu^{3+} ions in the LaPO_4 host, probably due to changes in the large surface-to-volume ratio and amounts of defects on particle's surfaces. Table 3 also presents values of radiative and nonradiative transition rates of Eu^{3+} in different size LaPO_4 , and values of internal quantum efficiencies that are calculated from transition rates. Results show that internal quantum yield is strongly influenced by particle's morphology and preparation method. The highest value is found for

nanorods (2 nm × 15 nm), and the lowest for 2 nm nanoparticles. It can be observed that Judd-Olfelt theory provides values of quantum efficiency that are slightly underestimated, since calculation does not account intensity of ${}^5D_0 \rightarrow {}^7F_{3,5}$ emissions. However, the obtained trend in values is not affected.

4. Conclusions

To conclude, four different methods of synthesis were used for preparations of Eu^{3+} -doped LaPO_4 and EuPO_4 phosphor particles of different sizes and morphologies: spherical nanoparticles of 2 nm, 5 nm and 100 nm in diameter, and short nanorods of 2–4 nm in diameter and 15–20 nm in length. It was found that the particle size has significant influence on the structure and luminescent properties of particles. In particular, with a decrease in particle diameter emission bands broaden due to structural disorder and new emission bands from defect states appear in ultrasmall (2 nm) particles. Moreover, no concentration quenching of Eu^{3+} emission was observed with ultrasmall nanoparticles and nanorods; these samples have more than 50% of atoms on their surface. Thus, these nanomaterials can be heavily doped with Eu, up to stoichiometric EuPO_4 . In larger particles concentration quenching occurs at 10 mol% doping level. Critical distance for energy transfer between Eu^{3+} ions is about 18.2 Å and discloses the dipole-dipole interaction as the dominant mechanism for the emission quenching.

Acknowledgments

The authors acknowledge the financial support of the Ministry of Education, Science and Technological Development of the Republic of Serbia (Projects nos. 45020 and 172056). T.G acknowledges to the ERDF PostDoc project No. 1.1.1.2/VIAA/1/16/215 (1.1.1.2/16/1/001).

References

- [1] X.F. Duan, Y. Huang, Y. Cui, J.F. Wang, C.M. Lieber, Indium phosphide nanowires as building blocks for nanoscale electronic and optoelectronic devices, *Nature* 409 (2001) 66–69.
- [2] H. Kind, H. Yan, B. Messer, M. Law, P. Yang, Nanowire ultraviolet photodetectors and optical switches, *Adv. Mater.* 14 (2002) 158–160.
- [3] X.Y. Kong, Y. Ding, R. Yang, Z.L. Wang, Single-crystal nanorings formed by epitaxial self-coiling of polar nanobelts, *Science* 303 (2004) 1348–1351.
- [4] M.Y. Guan, J.H. Sun, F.F. Tao, Z. Xu, A host crystal for the rare-earth ion dopants: synthesis of pure and Ln-doped urchin like BiPO_4 structure and its photoluminescence, *Cryst. Growth Des.* 8 (2008) 2694–2697.
- [5] M. Schäfer-Korting (Ed.), *Drug Delivery in Handbook of Experimental Pharmacology*, Springer-Verlag, Berlin Heidelberg, Germany, 2010.
- [6] L. Yan, R.B. Yu, J. Chen, X.R. Xing, Template-free hydrothermal synthesis of CeO_2 nano-octahedrons and nanorods: investigation of the morphology evolution, *Cryst. Growth Des.* 8 (2008) 1474–1477.
- [7] Z. Lu, J. Zhou, A. Wang, N. Wang, X. Yang, Synthesis of aluminium-doped ZnO nanocrystals with controllable morphology and enhanced electrical conductivity, *J. Mater. Chem.* 21 (2011) 4161–4167.
- [8] X. Chen, Z. Xia, M. Yi, X. Wu, H. Xin, Rare-earth free self-activated and rare-earth activated $\text{Ca}_2\text{NaN}_2\text{V}_3\text{O}_{12}$ vanadate phosphors and their color-tunable luminescence properties, *J. Phys. Chem. Solids* 74 (2013) 1439–1443.
- [9] T.V. Gavrilović, D.J. Jovanović, V. Lojpur, A. Nikolić, M.D. Dramićanin, Influence of $\text{Er}^{3+}/\text{Yb}^{3+}$ concentration ratio on the downconversion and up-conversion luminescence and lifetime in $\text{GdVO}_4:\text{Er}^{3+}/\text{Yb}^{3+}$ microcrystals, *Sci. Sinter.* 47 (2015) 221–228.
- [10] B. Shao, Z. Yang, Y. Wang, J. Li, J. Yang, J. Qiu, Z. Song, Coupling of Ag nanoparticle with inverse opal photonic crystals as a novel strategy for upconversion emission enhancement of $\text{NaYF}_4:\text{Yb}^{3+}, \text{Er}^{3+}$ nanoparticles, *ACS Appl. Mater. Interfaces* 7 (2015) 25211–25218.
- [11] L. Jiayan, Y. Zhengwen, W. Hangjun, Y. Dong, Q. Jianbei, S. Zhiguo, Y. Yong, Z. Dacheng, Y. Zhaoyi, Enhancement of the up-conversion luminescence of $\text{Yb}^{3+}/\text{Er}^{3+}$ or $\text{Yb}^{3+}/\text{Tm}^{3+}$ co-doped NaYF_4 nanoparticles by photonic crystals, *J. Mater. Chem. C* 1 (2013) 6541–6546.
- [12] X.Z. Xiao, B. Yan, Y.S. Song, $\text{GdP}_2\text{V}_1-x\text{O}_4:\text{Eu}^{3+}$ nanophosphor and hydrated $\text{Zn}_3(\text{PO}_4)_2:\text{Eu}^{3+}$ nanorod bunch: facile reproducible hydrothermal synthesis,

- controlled microstructure, and photoluminescence, *Cryst. Growth Des.* 9 (2009) 136–144.
- [13] Y.J. Zhang, H.G. Guan, The growth of lanthanum phosphate (rhabdophane) nanofibers via the hydrothermal method, *Mater. Res. Bull.* 40 (2005) 1536–1543.
- [14] A. Tymiański, T. Grzyb, Are rare earth phosphates suitable as hosts for upconversion luminescence? Studies on nanocrystalline REPO_4 ($\text{RE} = \text{Y}, \text{La}, \text{Gd}, \text{Lu}$) doped with Yb^{3+} and $\text{Eu}^{3+}, \text{Tb}^{3+}, \text{Ho}^{3+}, \text{Er}^{3+}$ or Tm^{3+} ions, *J. Lumin.* 181 (2017) 411–420.
- [15] F.H. Firsching, S.N. Brune, Solubility products of the trivalent rare-earth phosphates, *J. Chem. Eng. Data* 36 (1991) 93–95.
- [16] A. Rouanel, J.J. Serra, K. Allaf, V.P. Orlovskii, Rare-earth orthophosphates at high temperatures, *Inorg. Mater.* 17 (1981) 76–81.
- [17] N. Saltmarsh, G.A. Kumar, M. Kailasnath, Vittal Shenoy, C. Santhosh, D.K. Sardar, Spectroscopic characterizations of Er doped LaPO_4 submicron phosphors prepared by homogeneous precipitation method, *Opt. Mater.* 53 (2016) 24–29.
- [18] Y. Guo, P. Woznicki, A. Barkatt, E.E. Saad, I.G. Talmy, Sol-gel synthesis of microcrystalline rare earth orthophosphates, *J. Mater. Res.* 11 (1996) 639–649.
- [19] R.R. Kesavulu, Ch. Basavapoornima, C.S. Dwaraka Viswanath, C.K. Jayasankar, Structural and NIR to visible upconversion properties of Er^{3+} -doped LaPO_4 phosphors, *J. Lumin.* 171 (2016) 51–57.
- [20] R.P. Rao, D.J. Devine, RE-activated lanthanide phosphate phosphors for PDP applications, *J. Lumin.* 87–89 (2000) 1260–1263.
- [21] E.E. Boakye, P. Mogilevsky, R.S. Hay, Synthesis of nanosized spherical rhabdophane particles, *J. Am. Ceram. Soc.* 88 (2005) 2740–2746.
- [22] S. Gallini, J.R. Jurado, M.T. Colomer, Synthesis and characterization of monazite-type $\text{Sr}:\text{LaPO}_4$ prepared through coprecipitation, *J. Eur. Ceram. Soc.* 25 (2005) 2003–2007.
- [23] C.C. Yu, M. Yu, C.X. Li, X.M. Liu, J. Yang, P.M. Yang, J. Lin, Facile sonochemical synthesis and photoluminescent properties of lanthanide orthophosphate nanoparticles, *J. Solid State Chem.* 182 (2009) 339–347.
- [24] S. Gallini, J.R. Jurado, M.T. Colomer, Combustion synthesis of nanometric powders of LaPO_4 and Sr-substituted LaPO_4 , *Chem. Mater.* 17 (2005) 4154–4161.
- [25] M.T. Colomer, J.A. Diaz-Guillén, A.F. Fuentes, Nanometric Sr-doped LaPO_4 monazite: synthesis by mechanical milling, characterization, and water incorporation on its structure, *J. Am. Ceram. Soc.* 93 (2010) 393–398.
- [26] L. Xu, H. Wei, B. Dong, Y. Wang, X. Bal, G.L. Wang, Q. Liu, Electrospinning preparation and photoluminescence properties of lanthanum phosphate nanowires and nanotubes, *J. Phys. Chem. C* 113 (2009) 9609–9615.
- [27] Z. Wei, L. Sun, C. Liao, J. Yin, X. Jiang, C. Yan, Size-dependent chromaticity in $\text{YBO}_3:\text{Eu}$ nanocrystals: correlation with microstructure and site symmetry, *J. Phys. Chem. B* 106 (2002) 10610–10617.
- [28] Z.-G. Wei, L.-D. Sun, X.-C. Jiang, C.-S. Liao, C.-H. Yan, Correlation between size-dependent luminescent properties and local structure around Eu^{3+} ions in $\text{YBO}_3:\text{Eu}$ nanocrystals: an XAFS study, *Chem. Mater.* 15 (2003) 3011–3017.
- [29] K.Y. Jun, D.Y. Lee, Y.C. Kang, S.B. Park, Size-dependent luminescent properties of hollow and dense $\text{BaMgAl}_{10}\text{O}_{17}:\text{Eu}$ blue phosphor particles prepared by spray pyrolysis, *Korean J. Chem. Eng.* 21 (2004) 1072–1080.
- [30] V. Muhr, M. Buchner, T. Hirsch, D.J. Jovanović, S.D. Dolić, M.D. Dramićanin, O.S. Wolfbeis, Europium-doped GdVO_4 nanocrystals as a luminescent probe for hydrogen peroxide and for enzymatic sensing of glucose, *Sens. Actuators B* 241 (2017) 349–356.
- [31] T.V. Gavrilović, D.J. Jovanović, V. Lojpur, M.D. Dramićanin, Multifunctional Eu^{3+} - and $\text{Er}^{3+}/\text{Yb}^{3+}$ -doped GdVO_4 nanoparticles synthesized by reverse micelle method, *Sci. Rep.* 4 (2014) 4209–4217.
- [32] T.V. Gavrilović, D.J. Jovanović, K. Smits, M.D. Dramićanin, Multicolor upconversion luminescence of $\text{GdVO}_4:\text{Ln}^{3+}/\text{Yb}^{3+}$ ($\text{Ln}^{3+} = \text{Ho}^{3+}, \text{Er}^{3+}, \text{Tm}^{3+}, \text{Ho}^{3+}/\text{Er}^{3+}/\text{Tm}^{3+}$) nanorods, *Dyes Pigments* 126 (2016) 1–7.
- [33] T.V. Gavrilović, D.J. Jovanović, L.V. Trandafilović, M.D. Dramićanin, Effects of Ho^{3+} and Yb^{3+} doping concentrations and Li^{+} co-doping on the luminescence of GdVO_4 powders, *Opt. Mater.* 45 (2015) 76–81.
- [34] R. Zhou, M. Lv, X. Li, The effect of HNO_3 on morphology, phase transformation, and luminescence properties of $\text{LaPO}_4:\text{Eu}^{3+}$ phosphors, *Opt. Mater.* 51 (2016) 89–93.
- [35] H. Meyssamy, K. Riwozki, A. Kornowski, S. Nausied, M. Haase, Wet-chemical synthesis of doped colloidal nanomaterials: particles and fibers of $\text{LaPO}_4:\text{Eu}$, $\text{LaPO}_4:\text{Ce}$, and $\text{LaPO}_4:\text{Ce}, \text{Tb}$, *Adv. Mater.* 11 (1999) 840–844.
- [36] M. Yang, H. You, Y. Liang, J. Xu, F. Lu, L. Dai, Y. Liu, Morphology controllable and highly luminescent monoclinic $\text{LaPO}_4:\text{Eu}^{3+}$ microspheres, *J. Alloy. Compd.* 582 (2014) 603–608.
- [37] L. Peng, L. Yun, S. Xiaolei, G. Yaxin, Z. Gangqiang, Synthesis, characterization and luminescence properties of rod-like $\text{LaPO}_4:\text{Eu}^{3+}$ nanostructures, *J. Nanosci. Nanotechnol.* 16 (2016) 4012–4015.
- [38] M. Ferhi, K.H. Naifer, M. Ferid, Combustion synthesis and luminescence properties of $\text{LaPO}_4:\text{Eu}$ (5%), *J. Rare Earths* 27 (2009) 182–186.
- [39] H. Chen, Y. Ni, X. Ma, J. Hong, Pure monoclinic $\text{La}_{1-x}\text{Eu}_x\text{PO}_4$ micro-/nano-structures: fast synthesis, shape evolution and optical properties, *J. Coll. Interface Sci.* 428 (2014) 141–145.
- [40] M.J. Fisher, W. Wang, P.K. Dorhout, E.R. Fisher, Synthesis of $\text{LaPO}_4:\text{Eu}$ nanospheres using the sol-gel template method, *J. Phys. Chem. C* 112 (2008) 1901–1907.
- [41] X. Huang, Preparation and luminescence characteristics of monazite $\text{Eu}^{3+}:\text{LaPO}_4$ nanocrystals in NH_4NO_3 molten salt, *Opt. Mater.* 50 (2015) 81–86.
- [42] D. Wang, Q. Shun, Y. Wang, Z. Zhang, Synthesis and VUV luminescent properties of $\text{LaPO}_4:\text{Eu}^{3+}$ nanowires, *Mater. Chem. Phys.* 147 (2014) 831–835.
- [43] L.V. Vu, D.T.M. Huong, V.T.H. Yen, N.N. Long, Synthesis and optical characterization of samarium doped lanthanum orthophosphate nanowires, *Mater. Trans.* 56 (2015) 1422–1424.
- [44] Z.J. Zhang, X.D. Zheng, Z.C. Shi, X. Wang, Effect of Sm^{3+} concentration on the

- vibrational and luminescent properties of LaPO₄, Mater. Sci. Forum 848 (2016) 482–488.
- [45] D.M. Pimpalshende, S.J. Dhoble, Synthesis and luminescent performance of LaPO₄:Dy nanophosphor, Adv. Mat. Lett. 5 (2014) 688–691.
- [46] J. Dexpert-Ghys, R. Mauricot, M.D. Faucher, Spectroscopy of Eu³⁺ ions in monazite type lanthanide orthophosphates LnPO₄, Ln = La or Eu, J. Lumin. 69 (1996) 203–215.
- [47] D.T. Lien, D.T.M. Huong, L.V. Vu, N.N. Long, Structure and photoluminescence characterization of Tb³⁺-doped LaPO₄ nanorods prepared via the microwave-assisted method, J. Lumin. 161 (2015) 389–394.
- [48] D. Hou, X. Guo, C. Liu, T.-K. Sham, H. Liang, J. Gao, X. Sun, B. Zhang, F. Zhan, Y. Huan, Y. Tao, Hydrothermal synthesis, X-ray absorption and luminescence properties of Tb³⁺ doped LaPO₄, J. Lumin. 165 (2015) 23–29.
- [49] D.T.M. Huong, L.T. Trang, L.V. Vu, N.N. Long, Structural and optical properties of terbium doped lanthanum orthophosphate nanowires synthesized by hydrothermal method, J. Alloy. Compd. 602 (2014) 306–311.
- [50] H. Dong, Y. Liu, P. Yang, W. Wang, J. Lin, Controlled synthesis and characterization of LaPO₄, LaPO₄:Ce³⁺ and LaPO₄:Ce³⁺, Tb³⁺ by EDTA assisted hydrothermal method, Solid State Sci. 12 (2010) 1652–1660.
- [51] W.L. Dong, X.Y. Zhang, H. Shi, X.Y. Mi, N.L. Wang, K.X. Han, Synthesis and photoluminescence properties of LaPO₄:Ce³⁺, Tb³⁺ nanophosphors by microwave-assisted co-precipitation method at low temperature, Funct. Mater. Lett. 8 (2015) (1550078, 4 pp).
- [52] C.C. Alves, J. Demoucron, B. Caillier, P. Guillot, R. Mauricot, J. Dexpert-Ghys, J.M.A. Caiut, Amino acid coupled to Pr³⁺ doped lanthanum orthophosphate (LaPO₄) nanoparticles, Mater. Lett. 137 (2014) 435–439.
- [53] A.O. Chauhan, A.B. Gawande, S.K. Omanwar, Narrow band UVB emitting phosphor LaPO₄:Gd³⁺ for phototherapy lamp, Optik 127 (2016) 6647–6652.
- [54] N.P. Shaik, N.V.P. Rao, K.V.R. Murthy, Photoluminescent properties of LaPO₄:Gd³⁺ phosphor, Adv. Appl. Sci. Res. 5 (2014) 260–266.
- [55] D. Wang, Y. Wang, Luminescence properties of LaPO₄:Tb³⁺, Me³⁺ (Me = Gd, Bi, Ce) under VUV excitation, Mater. Res. Bull. 42 (2007) 2163–2169.
- [56] J. Cybinska, M. Guzik, C. Lorbeer, E. Zych, Y. Guyot, G. Boulon, A.-V. Mudring, Design of LaPO₄:Nd³⁺ materials by using ionic liquids, Opt. Mater. 63 (2017) 76–87.
- [57] T. Grzyb, A. Gruszczyka, S. Lis, Up-conversion luminescence of Yb³⁺ and Er³⁺ doped YPO₄, LaPO₄ and GdPO₄ nanocrystals, J. Lumin. 175 (2016) 21–27.
- [58] S.H. Yang, J.H. Yan, C.K. Yang, C.M. Lin, Luminescence of CNT coated LaPO₄:Tm phosphors and their field emission lamp application, J. Alloy. Compd. 612 (2014) 210–214.
- [59] S. Phadke, J.C. Ninob, M.S. Islam, Structural and defect properties of the LaPO₄ and LaP₅O₁₄-based proton conductors, J. Mater. Chem. 22 (2012) 25388–25394.
- [60] K. Riwozki, H. Meyssamy, A. Kornowski, M. Haase, Liquid-phase synthesis of doped nanoparticles: colloids of luminescing LaPO₄:Eu and CePO₄:Tb particles with a narrow particle size distribution, J. Phys. Chem. B 104 (2000) 2824–2828.
- [61] A. Phuruangrat, N. Ekthammathat, S. Thongtem, T. Thongtem, Preparation of LaPO₄ nanowires with high aspect ratio by a facile hydrothermal method and their photoluminescence, Res. Chem. Intermed. 39 (2012) 1363–1371.
- [62] I.E. Kolesnikov, A.V. Povolotskiy, D.V. Mamonova, E. Lähderanta, A.A. Manshina, M.D. Mikhailov, Photoluminescence properties of Eu³⁺ ions in yttrium oxide nanoparticles: defect vs. normal sites, RSC Adv. 6 (2016) 76533–76541.
- [63] B.R. Judd, Optical absorption intensities of rare-earth ions, Phys. Rev. 127 (1962) 750–761.
- [64] G.S. Ofelt, Intensities of crystal spectra of rare-earth ions, J. Chem. Phys. 37 (1962) 511–520.
- [65] Lj Đaćanin, S.R. Lukić, D.M. Petrović, M. Nikolić, M.D. Dramićanin, Judd–Ofelt analysis of luminescence emission from Zn₂SiO₄:Eu³⁺ nanoparticles obtained by a polymer-assisted sol–gel method, Physica B 406 (2011) 2319–2322.
- [66] W.T. Carnall, P.R. Fields, K. Rajnak, Electronic energy levels in the trivalent lanthanide aquo ions. I. Pr³⁺, Nd³⁺, Pm³⁺, Sm³⁺, Dy³⁺, Ho³⁺, Er³⁺, and Tm³⁺, J. Chem. Phys. 49 (1968) 4424–4442.
- [67] K. Binnemans, Interpretation of europium (III) spectra, Coord. Chem. Rev. 295 (2015) 1–45.
- [68] D. Uma Maheswari, J.S. Kumar, L.R. Moorthy, K. Jang, M. Jayasimhadri, Emission properties of Eu³⁺ ions in alkali tellurofluorophosphate glasses, Physica B 40 (2008) 1690–1694.
- [69] J.C. Boyer, F. Vetrone, J.A. Capobianco, A. Speghini, M. Bettinelli, Variation of fluorescence lifetimes and Judd–Ofelt parameters between Eu³⁺ doped bulk and nanocrystalline cubic Lu₂O₃, J. Phys. Chem. B 108 (2004) 20137–20143.
- [70] C. Liu, J. Liu, K. Dou, Judd–Ofelt intensity parameters and spectral properties of Gd₂O₃:Eu³⁺ nanocrystals, J. Phys. Chem. B 110 (2006) 20277–20281.
- [71] M. Kumar, T.K. Seshagiri, S.V. Godbole, Fluorescence lifetime and Judd–Ofelt parameters of Eu³⁺ doped SrBPO₅, Phys. Rev. B: Condens. Matter 410 (2013) 141–146.
- [72] M.G. Brik, Ž.M. Antić, K. Vuković, M.D. Dramićanin, Judd–Ofelt analysis of Eu³⁺ emission in TiO₂ anatase nanoparticles, Mater. Trans. 56 (2015) 1416–1418.